Energy, Environmental, and Catalysis Applications

Substrate Engineered Interconnected Graphene Electrode with Ultra High Energy and Power Densities for Energy Storage Applications

Ardalan Chaichi, Ying Wang, and Manas Ranjan Gartia

ACS Appl. Mater. Interfaces, **Just Accepted Manuscript** • DOI: 10.1021/acsami.8b03020 • Publication Date (Web): 01 Jun 2018

Substrate Engineered Interconnected Graphene Electrode with Ultra High Energy and Power Densities for Energy Storage Applications

Ardalan Chaichi[1], Ying Wang[1], Manas Ranjan Gartia[1,*]

[1]Department of Mechanical and Industrial Engineering, Louisiana State University, Baton Rouge, Louisiana 70803 USA

*Corresponding author: mgartia@lsu.edu

Abstract

Supercapacitors combine the advantages of electrochemical storage technologies like high energy density batteries and high power density capacitors. At 5-10 Wh Kg^{-1},[1] the energy densities of current supercapacitors are still significantly lower than energy densities of lead acid (20-35 Wh Kg^{-1}),[1-2] Ni-metal hydride (40-100 Wh Kg^{-1})[1] and Li-ion (120-170 Wh Kg^{-1})[3] batteries. Recently, graphene based supercapacitors have shown energy density of 40-80 Wh/kg.[1] However, their performance is mainly limited due to the reversible agglomeration and restacking of individual graphene layers caused by π-π interactions. The restacking of graphene layers leads to significant decrease of ion-accessible surface area and the low capacitance of graphene based supercapacitors. Here, we introduce a microstructure substrate based method to produce fully delaminated and stable interconnected graphene structure using flash reduction of GO in a few seconds. With this structure, we achieve the highest amount of volumetric capacitance obtained so far by any type of pure carbon based material. The affordable and scalable production method is capable of producing electrodes with energy density of 0.37 Wh cm^{-3} and power density of 416.6 W cm^{-3}. This electrode maintained more than 91 % of its initial capacitance after 5000 cycles. Moreover, combining with ionic liquid, this solvent free graphene electrode material is highly promising for on-chip electronics, micro supercapacitors as well as high power applications.

Keywords: Interconnected graphene network; Energy storage; Supercapacitor; GO flash reduction; Substrate patterning

1. Introduction

Supercapacitors and batteries are known as two fundamental technologies for electrochemical energy storage purposes. Although batteries provide considerably high energy densities (100-243 Wh kg^{-1}),[1-2] they suffer from extremely low power densities (10-100 W kg^{-1})[1-3] that result in several hour recharging times. On the other hand, supercapacitors offer fast recharging times (minutes or even seconds), albeit lower energy densities compared to batteries. However, coupling batteries with supercapacitors has been accomplished in practical applications, such as electric automobiles, to benefit from the advantages of both products.[4-8] Therefore, creating a material for electrochemical energy storage devices that can handle a high energy density as well as maintaining a high power density is contemplated revolutionary.[9] This combination is not achievable, unless novel architectures are created in micro and nano scale to manipulate the common properties of current materials.[7, 10-13] In practical applications, several micro grams of active material per unit area of electrode is required to maintain stable charge/discharge cycles and high reliability. Nevertheless, nano and micro scale engineered materials cannot be simply scaled up to more than one micro gram per unit area due to the drastic decline of charge storage and charge transfer in electrochemical configurations caused by diffusion constraints.[14-15] This limitation can be overcome by providing accessibility for electrolyte throughout the active material which is ignored in the vast majority of studies and publications.[16-18] Being unable to wet the micro pores within active material by electrolyte, decreases the probability of successful double layer formation in porous materials which results in dramatic drop in double layer capacitance as well as the charge/discharge rate.[9, 19] Consequently, carbon based materials, such as activated carbon, nanotubes and graphene, demonstrate much lower double layer capacitance compared to their theoretical values.[1, 3, 9] In addition to the unaffordable price of vertically grown carbon nanotubes, to use carbon nanotubes in practical applications, further addition of conductive polymers is necessary for the formation of a pseudocapacitance pair.[20-21] Otherwise, the amount of capacitance achieved by CNT supercapacitors is considerably low and ineffective.[1-3] Meanwhile, the formation of pseudocapacitance is unfavorable in many applications because of the high rate of capacitance decay.[9, 22] On the contrary, highly porous structure of interconnected graphene network with

distinguished electron transfer characteristics is capable of providing an ideal architecture for the manufacturing of ultra-high electrical double layer capacitance due to prevailing diffusion limits of ubiquitous carbon based electrodes.[10-11, 23-25] The presence of meso and micro porous morphology through the interconnected graphene network increases the capability of charge storage as well as maintaining high power density. Electrochemical capacitance for the aforementioned structure can even exceed the value for single layer graphene (550 F g^{-1})[23, 26-30] which has been known as the most ideal type of graphene for energy storage applications. However, interconnected graphene network demonstrates its superior properties while the graphene layers are delaminated and stabilized in this structure. Although the easy accessibility of surfaces and edges on graphene sheets by electrolyte can be considered as the mechanism behind the superiority of this structure over other types of common carbon based materials, the extreme restacking propensity of graphene layers restricts their double layer capacitance.[4, 23, 31] Thus, taking advantage of the entire potential of this material for energy storage devices is limited. The accessibility of graphene edge planes plays a significant role even in the electrochemical capacitance of other types of graphitic materials like nanotubes. There is a direct relation between the number of available graphene edge sites and double layer capacitance for all types of graphitic nanomaterials.[9, 32]

The curved structure of graphene sheets provide a vast wettable surface for the electrolyte that requires to be engineered and manipulated for practical energy storage capacitors. Accordingly, the creation of single layer graphene by various chemical and mechanical methods attracted a lot of interest for energy storage devices.[16, 26, 29, 33-37] Meanwhile, the production of single layer graphene with fairly good quality is extremely expensive and totally impractical for mass production.[26, 32] Therefore, many efforts have been put into creating delaminated interconnected graphene morphologies. Graphene electrodes that were produced by exfoliation of graphene oxide exhibited the specific capacitance of 100-117 F g^{-1} in 1M H_2SO_4 at the scan rates of 0.01 - 1 V s^{-1}.[9] The results of this study showed that the capacitance of multi layered graphene can be superior to carbon nanotubes and onion-like carbon.[1, 9] However, it is still lower than carbide derived carbon, activated carbon and zeolite templated carbon.[4, 9] Therefore, endeavors to reduce the agglomeration of graphene layers to achieve higher capacitance, close to the theoretical values, have been started in last few years.[2] Reduction of graphene oxide in hydrazine gaseous media was among the first efforts that resulted in specific capacitance of 205

F g^{-1} in 0.3 KOH electrolyte that decreased dramatically after several cycles.[9] Another approach was to positively charge the graphene surface during reduction procedure by means of p-phenylenediamine (PPD).[3, 9] However, these methods did not demonstrate favorable results in energy storage applications.[1, 9] Preparation of stabilized graphene in aqueous environment is another technique that benefits from aromatic interaction mechanisms and impressively increased the suspension stability of graphene layers and formation of double layer capacitance (~120 F g^{-1}).[9] Decreasing the size of graphene segments is another suggested method to reduce the agglomeration of layers and resulted in increased electrochemical capacitance from 82 to 132 F g^{-1} in 1M H_2SO_4 electrolyte.[9, 38] Curved mesoporous graphene has demonstrated promising specific capacitance (100-250 F g^{-1}) in ionic liquids, albeit, accompanied with poor stability and reliability.[1-2] Thermal exfoliation of graphene oxide has been reported to produce electrodes with specific capacitance more than 200 F g^{-1}, although with very poor stability.[38] Several reports studied the creation of mesoporous graphene like holey graphene,[12] graphene oxide hydrogels,[39] nitrogen doped carbon paper[40] and 3D porous graphene[41] by use of functional groups that demonstrates high pseudocapacitance which is detrimental for many applications mostly because of the low volumetric capacitance.[20-21, 28, 42-47]

Recently, laser and flash reduction of graphene oxide have been employed to prepare carbon based electrodes for electrochemical energy storage applications.[16, 21-22, 47-53] However, in these studies the importance of vital parameters like interlayer spacing and the effect of supporting substrate topography on the capacitance were not explored. In the current study, we present a novel method for production of highly delaminated graphene network that activates the exceptional potentials of interconnected graphene structure for several energy applications. Controlling the spacing between graphene layers as well as the topography of inactive substrate are significant factors which are capable of exhibiting full potential of layered graphene structure and have been mostly ignored in previous studies.

2. Experimental Section

Fabrication of substrate: High quality graphene oxide (GO) (Graphenea Inc., Cambridge, MA) was dispersed in water with the monolayer content of >95% and concentration of 4 mg mL^{-1}. In order to exfoliate agglomerated stacks of GO, the precursor was treated in ultrasonic bath for 30 minutes. Transparent polyethylene terephthalate (PET) was used as substrate for

producing the electrochemical electrodes. For creating nano and micro patterns on the plastic substrate, replica molding process was used. Master molds were made by laser interference lithography on quartz substrate and they were silanized for 30 min to become hydrophobic. 2 ml of UV-curable polymer (NOA-61, Sigma Aldrich) were dropped on the surface of master mold with a PET sheet on top of it. Afterwards, it was exposed to UV light with the power of 210 mW cm^{-2} for 1 min. Periodic patterns are formed on PET once the UV-curable polymer is fixed. The plastic is then peeled off gently from the master mold (Fig. S1).

Fabrication process of laser and flash reduced graphene electrodes: For the production of flash reduced graphene, 20 ml of GO were drop-cast on the surface of patterned and flat plastic substrates and dried over night at room temperature. A xenon digital camera flash (Neewer PRO i-TTL) was used in air and ambient conditions for reduction of GO to graphene. The flash energy was approximately 0.1-2 J cm^{-2} that was measured by Gentec QE25ELP-S-MB-INT-D0 light measurement system. After flashing, the golden-brown color of GO turns to black which is an evidence for successful reduction of GO to graphene. In order to make laser reduced samples, LG lightscribe DVD burner employed by means of a regular lightscribe software. Drop-cast GO on PET substrate was glued to the top surface of a lightscribe DVD and burnt in DVD optical drive. Although it takes around 20 min for each cycle, the process should be repeated for at least six times to achieve an acceptable amount of graphene out of GO. Thus, all the laser reduced samples in this study were burnt for eight times. After the preparation of electrodes, three electrode configuration tests were performed in 0.5 M H_2SO_4 electrolyte with Pt and Hg/Hg^+ as working and reference electrodes, respectively. Fabricated electrodes were named LR (laser reduced), FR (flash reduced on flat substrate), FRNS (flash reduced on nano-patterned substrate) and FRMS (flash reduced on micro-patterned substrate).

Electrochemical Experiments: Sandwich type devices were also made out of LR, FR, FRNS and FRMS electrodes by means of microporous membrane and 0.5M H_2SO_4 electrolyte. Electrochemical tests including cyclic voltammetry (CV) and galvanostatic charge/discharge were performed by CHI 600E electrochemical workstation. Electrochemical Impedance Spectroscopy (EIS) measurements were carried out with amplitude of 0.005 V AC in the range of 0.01 Hz to 100 kHz. Volumetric capacitance was calculated using equation 1,[42] where υ, i, ΔV

and v are defined as scan rate (V s^{-1}), applied current (A), sweep potential window (V) and volume of active material (cm^3), respectively.

$$C_v = \frac{\int i.dV}{v.\Delta V.\upsilon} \quad (1)$$

For calculating volumetric capacitance (F cm^{-3}) from the charge/discharge diagrams, equation 2[42] was used.

$$C_v = \frac{-idt}{vdV} \quad (2)$$

Specific energy density E (Wh cm^{-3}) and power density P (W cm^{-3}) were calculated using equation 3 and equation 4,[44] where t is the discharge time excluding IR drop.

$$E = \frac{C_v \times (\Delta V)^2}{3600} \quad (3)$$

$$P = \frac{E \times 3600}{\Delta t} \quad (4)$$

Conductivity of laser and flash reduced GO was measured by performing cyclic voltammetry (CV) tests in the potential window of -1 to 1 V and scan rate of 0.1 V s^{-1}. The electrical conductivity of GO surface was measured (Fig. S3) to be 6.38 x 10^{-4} S m^{-1}. After laser and flash reduction, electrical conductivity increased to 1.40 x 10^3 S m^{-1} and 2.14 x 10^3 S m^{-1}, respectively.

General Characterizations:

Morphological, Energy-dispersive spectroscopy (EDS) and cross sectional studies were performed by scanning electron microscopy (Quanta 3D DualBeam FEG FIB-SEM). X-ray diffraction diagrams were performed by using Panalytical Empyrean multipurpose diffractometer. In order to study the surface properties, ANASYS atomic force microscope (AFM) has been employed. Renishaw inVia confocal Raman microscope was used to achieve the Raman spectrum of samples. All the spectra were acquired by the excitation wavelength of 532 nm in the range of 500 to 3000 cm^{-1}. For X-ray photoelectron spectroscopy (XPS) analysis, Scienta Omicron ESCA 2SR instrument was employed. It was equipped with a monochromatic Al Kα X-ray source of 1486.7 eV. Altamira AMI-200 was employed for BET experiments. 1 mg of samples were used for surface area measurements and further calculations.

3. Results and discussions

Figure 1 schematically shows the formation of interconnected graphene layers on top of flat, nano and micro-structure patterned substrates. A xenon digital camera flash was used to produce the graphene from graphene oxide (GO) (see Fig. S1 for details). The fabricated electrodes were named FR (flash reduced on flat substrate), FRNS (flash reduced on nano-patterned substrate) and FRMS (flash reduced on micro-patterned substrate). In order to compare the performance of the flash-reduced electrodes, GO was also reduced using lightscribe DVD technique to produce graphene and named LR (laser reduced). Figures 2a and 2b show the cross-sectional SEM images of LR and FR graphene structure, respectively. We analyzed the distance between graphene layers at ten different places on each sample (Fig. S2). The LR sample shows an average spacing of 0.25 μm and the FR sample shows an average spacing of 1.76 μm. Delamination of interconnected multi layered graphene structure benefits electrochemical devices by providing a highly porous architecture that facilitates the wettability of active material and results in rapid ion transfer and enabling more surface for the formation of double layer capacitance. Color change from brown (for GO) to black (for LR and FR) can be considered as the first evidence for the successful conversion of GO to graphene which is shown in figure 2c. We also measured the electrical surface resistance of the device before and after the reduction process. The electrical conductivity of GO surface was measured to be 6.38×10^{-4} S m^{-1} and after reduction (Fig. S3), the conductivity increased to 1.40×10^{3} S m^{-1} and 2.14×10^{3} S m^{-1} for LR and FR process, respectively. Another parameter that affects the overall functionality of graphene based supercapacitors is the amount of GO converted to graphene during the conversion process when using GO as the starting material. Figure 2d shows the XRD results for the LR and FR samples. A thin layer of Vaseline was used to adhere LR sample to sample holder and keep it flat. The results were compared with the XRD of graphite, graphene, and GO. The XRD pattern of FR shows two characteristic peaks. The broad peak at $2\theta = 26^{o}$ with a *d*-spacing of 3.42 A^{o} is generally associated with the graphitic peak.[54-56] The other peak occurred at the same position as that of LR sample's characteristic peak. The XRD pattern of LR shows characteristic peak of $2\theta = 10.09^{o}$ which corresponds to a *d*-spacing of 8.76 A^{o}. This peak is generally associated with graphene oxide.[54-56] The oxygen containing functional groups in GO are responsible for the increased *d*-spacing seen in the XRD of LR samples.[57-59] Some conclusion can be drawn from the intensity ratio of peak of 2θ in the XRD results about which sample has

higher oxygen containing functional groups. LR graphene XRD structure shows a considerable amount of residual graphene oxide ($I_{GO}/I_{Graphene} \approx 11.14$, I_{GO}: intensity of GO peak, $I_{Graphene}$: intensity of graphene peak) compared to FR graphene structure ($I_{GO}/I_{Graphene} \approx 0.77$). This residual GO negatively influences the electrochemical properties of supercapacitors and reduces the amount of capacitance achievable by the device to much lower values. Therefore, the amount of GO conversion should be taken into consideration before using such material in an application regardless of the chosen method for GO reduction. Raman spectrum of laser and flash reduced samples are provided in figures 2e and 2f. First of all, the appearance of 2D peaks at ~ 2651 cm^{-1} in the Raman spectra of LR and FR samples is another evidence of the conversion of GO to graphene (2D peak is absent in the GO Raman spectrum) (Fig. 2e). The G-band and D-band appears for all the samples. The G-band of LR (1572 cm^{-1}) and FR (1581 cm^{-1}) samples moved to a lower frequency compared to G-band of GO (1585 cm^{-1}) sample. This indicates topological disordering of two-dimensional graphene layers and formation of three-dimensional structures in FR samples. Another indication of three-dimensional structure formation can be derived from the change in I_D/I_G ratio. The I_D/I_G intensity ratio of GO was 0.93 and increased to 1.07 for LR, and further increased to 1.16 for the FR sample. It indicates reduction of the grain size of the sp^2 domains while keeping the aromatic ring intact during the reduction of GO,[60] and the elimination of oxygen functional groups.[61] Similar observations were also reported for reduced GO in previous literatures.[62] The G-band represents in-plane stretching mode vibration of sp^2 sites (double bond carbon atoms) and D-band represents breathing mode vibration of sp^2 sites. More number of phonons participate in the vibration due to decrease in grain size and hence the intensity of G-band decreases. Since the linewidth of D and G peaks are different in all the samples, the 1st order Raman spectra were deconvoluted by three peaks: two of those peaks appeared at D and G-band positions and the third peak is denoted as D*. The D* peak is interpreted as the amorphous sp^3 content (for example, single bond carbon as C-OH).[63-64] Figure 2f shows the positions of D* band: GO (1563.5 cm^{-1}, FWHM = 80.9 cm^{-1}), LR (1510.4 cm^{-1}, FWHM = 99.8 cm^{-1}), and FR (1498.7 cm^{-1}, FWHM = 127.9 cm^{-1}). According to Claramunt et al.,[64][48] with decrease in oxygen content, the D* peak moves toward lower frequencies (wavenumbers). Compared to GO (1563.5 cm^{-1}), the D* peak moved to a lower frequency for the FR samples (1498.7 cm^{-1}). It provides further confirmation that for FR sample, the oxygen content is decreasing compare to both GO and LR samples.

Further study were performed to understand the effect of supporting substrate on the interlayer spacing and the performance of electrochemical device. Three differently patterned plastic substrates were used to convert GO to graphene using flash reduction technique. For FR specimen that was exposed to flash light on a non-patterned substrate, bottom graphene layers at the interface of active material and substrate are found to be compressed (Fig. 3a). Delamination of graphene layers occurred only for the top layers, about 2 μm above the substrate. Meanwhile, interconnected graphene structure were found to be highly delaminated right above the substrate when GO was reduced on patterned substrates (nano and micro substrates) (Figs. 3b, 3c). The results can be explained by the fact that nano and micro substrates provide extra space for the expansion of layers and allow escape route for the oxygen gas generated during the GO reduction process. It is noteworthy to mention that the delamination of graphene sheets is more clearly visible when the size of patterns increases from hundreds of nanometers to few microns. Our analysis shows that the average graphene interlayer distance increased from 0.8 μm to 2.2 μm while using micro patterned structure instead of non-patterned structure (figures 3a-c). Figures 3d, 3e and 3f show the surface of drop-cast GO which was in contact with micro and nano patterned substrates. Accordingly, the periodic structures are clearly visible by means of SEM and AFM microscopes. The inset of Fig. 3d and Fig. 3e show the SEM of micro and nano structure. The microstructure is inverse pyramid shaped with pitch of 2 μm and depth of 1.2 μm. The nanostructure is nanohole periodic structure with pitch of 350 nm, hole diameter of 180 nm and hole depth of 500 nm.

Figure 4a illustrates the X-ray energy dispersive spectrum (EDS) analysis results obtained for different type of samples inside the SEM to determine the amount of residual oxygen which is directly correlated to residual GO (also see Fig. S4). For all the samples three prominent peaks were observed. The peak at around 0.270 keV is assigned to C, the peak at 0.521 keV is assigned to O, and the peak at 2.06 keV is due to the Pt (used in SEM to reduce charging effect during imaging). From the analysis, LR specimen showed the highest value of residual oxygen (39.8 at.%) (Fig. 4c). The flash reduction of GO on micro patterned substrate (FRMS) dramatically decreases the residual oxygen to 4.2 at.%. Thus, the presence of micro and nano structure on substrate surface during GO reduction process, enhances oxygen depletion which results in an expanded interconnected network of graphene. In order to provide further evidence about the difference in the oxygen content, high-resolution XPS C 1s spectrum analysis

has been performed for all the samples. By means of this technique, surface chemical properties of carbon and oxygen atoms can be investigated. The XPS C 1s spectra for LR, FR, FRNS and FRMS samples were shown in Fig. 4c (i)-(iv) respectively. All the spectrum were deconvoluted into four distinct peaks (FRNS and FRMS showed only three peaks). Distinctive peak shapes and identities clearly demonstrate different surface properties among LR, FR, FRNS and FRMS samples. The XPS peak positions and the corresponding bond assignment are as follows: LR sample has peak at 284.38 eV (C=C), 286.54 eV (C-OH, C-O-C), 287.35 eV (O-C=O), and 288.06 eV (C=O); FR sample has peak at 284.39 eV (C=C), 285.33 eV (C-C, sp^3 C), 285.77 eV (C-O), 288.96 eV (O-C=O); FRNS has peak at 284.6 eV (C=C), 285.54 eV (C-C), 288.47 eV (O-C=O); FRMS has peak at 284.4 eV (C=C), 284.61 eV (C=C) and 285.18 eV (C-C, sp^3 C). The assignment of the bonds are in agreement with the literature values.[43] Yang et al. reported previously that laser reduction method of graphene oxide is not capable of removing oxygen-containing functional groups efficiently.[43] Remarkably, FRMS process removed most of the oxygen containing functional groups compared to other synthesis methods. From XPS analysis, oxygen content of LR, FR, FRNS and FRMS samples were found to be 34.3, 29.9, 15.9 and 4.9 at.%, respectively, which are in close agreement with the values found from the EDS analysis (Fig. 4c). The decrease in oxygen content in FRNS and FRMS samples demonstrate that employing flash reduction technique on nano and micro structured substrates leads to enhanced conversion of GO to graphene (also see Fig. S10).

In order to understand the effect of morphological changes of graphene layers on the electrochemical behavior of electrodes, cyclic voltammetry (CV) tests were performed on the samples. Figure 5 and Fig. 6 demonstrate the results obtained from electrochemical response of LR, FR, FRNS and FRMS samples. The CV curves (Fig. 5) were reported for a scan rate of 100 mV s^{-1} and normalized by the volume of the film (see Fig. S5 for volume measurement details). The rectangular symmetric shape of the CV curve for FRMS indicates formation of electric double layer (EDL) capacitor. The increase of specific current (current per unit volume) for FRMS device with increase of scan rate from 10 mV s^{-1} to 300 mV s^{-1} (Fig. S6) indicates fast charge propagation within the electrode. Further, LR sample showed a peak current density of 80 mA cm^{-3}. The FRMS sample showed two-order of magnitude higher current density (15,000 mA cm^{-3}) compared to LR devices. The volumetric capacitance is estimated using two methods: (1) from the integration of CV curves, and (2) from the galvanostatic charge/discharge curve. The

volumetric capacitance of LR, FR, FRNS and FRMS electrodes were calculated using the relation[42] $C_v = \frac{\int I.\mathrm{d}V}{\mathrm{v}.\Delta V.\nu}$, where C_v = volumetric capacitance (F cm^{-3}), I = voltammetric current (A), v = volume (cm^3) of the device, ΔV= sweep potential window (V) and ν= scan rate (V s^{-1}). The volumetric capacitance of LR, FR, FRNS and FRMS electrodes were found to be 3.7 F cm^{-3}, 178.7 F cm^{-3}, 441.5 F cm^{-3} and 1205.2 F cm^{-3}, respectively. The galvanostatic charge/discharge (GC) curves were performed at a constant current density of 100 mA cm^{-3} and shown in Figure 6a. The triangular shape of the GC curve indicates fast ion transport and efficient EDL formation within the supercapacitor electrodes. The volumetric capacitance of the different supercapacitor designs were calculated from the galvanostatic charge/discharge values using the equation[42] $C_v = \frac{I}{\mathrm{v}(-dV/dt)}$. The volumetric capacitance obtained by charge/discharge curves were estimated to be 3.8 F cm^{-3} (LR), 180.7 F cm^{-3} (FR), 450.1 F cm^{-3} (FRNS) and 1224.4 F cm^{-3} (FRMS). The volumetric capacitance values estimated by the two methods are in agreement with each other. The IR drop (voltage drop at the start of each discharge curve) was measured to be ~ 0.01 V at 100 mA cm^{-3}indicating very low resistance for all the devices. The corresponding results for three-electrode test were shown in Fig. S7. From both CV and charge/discharge diagrams, order of magnitude differences in volumetric capacitance values were observed for the FRMS devices, mainly due to the removal of residual oxygen containing functional groups and the increase in the interlayer spacing originated from adopting different synthesis method. Therefore, such major improvements can be obtained from exact same precursors by solely manipulating and engineering the electrode materials. Figure 6a shows that 324x higher volumetric capacitance can be obtained from flash reduction of GO (FRMS devices) compared to laser scribing (LR devices) by just manipulating the geometry of the supporting substrate. Furthermore, reducing GO by laser scribe drive takes several hours for producing acceptable amount of graphene, while much higher quality graphene structure can be produced in less than a second by flash reduction technique.

Utilizing patterned substrates (FRNS and FRMS) instead of a flat surface (FR) also provided high specific capacitance. The specific capacitance was calculated using the equation: $C_s = \frac{I}{m(-dV/dt)}$, where m is the active mass within the device. The active mass was calculated using two methods: (1) by weighing the sample after GO reduction and subtracting the weight of

the substrate, (2) using SEM to calculate the volume and estimating the mass using the density of graphene. The specific capacitance of FRMS was calculated to be 680.2 F g^{-1} at a current density of 100 mA cm^{-3}, which is higher than the theoretical value of 552 F g^{-1} reported for single layer graphene (it should be noted that the theoretical value is calculated from the single-layer graphene intrinsic capacitance[27] value of ~ 21 μF cm^{-2}, and specific surface area of graphene[29-30, 36, 65-66] ~ 2630 m^2 g^{-1}). Due to the use of reduced GO and existence of residual oxygen in the samples, pseudocapacitance and double layer capacitance both contribute to the total capacitance value.[1-2] As a result, the achieved capacitance for FRMS sample is higher than the theoretical value. Correspondingly, interconnected graphene network produced by a low-cost material like GO, provides quite higher specific capacitance than a single layer graphene which has been presumed to possess the highest electrochemical capacitance among different types of graphene. Further, micro structure patterned electrode (FRMS) demonstrated 172% higher volumetric capacitance compared to the nano structured graphene electrode (FRNS). This can be explained by the ~ 51% higher inter layer spacing of graphene sheets and ~ 14.5x greater conversion of GO to graphene on FRMS samples compared to FRNS. BET results showed that FRMS sample has specific surface area of 1262.3 m^2 g^{-1}, which is about four-fold higher ion accessible area compared to 355.8 m^2 g^{-1} found for GO samples (Fig. S8). A further confirmation of fast ion transport in FRMS device is supported by the electrochemical impedance spectroscopy (EIS) results shown in Fig. 6b. At low frequency the curve for FRMS showed large slope with sharp (90^o) rise, indicating high accessible surface area in the graphene film. At higher frequency, the intercept of the Nyquist plot can be utilized to measure the internal and charge transfer resistance. The FRMS device showed the least internal resistance among the different tested designs and found to be 5.8 Ω cm^{-2} compared to 10340 Ω cm^{-2} measured for LR. In addition, the FRMS showed quite small charge transport resistance with an almost invisible semicircle, demonstrating the superiority of the device by retaining capacitive behavior even at higher frequencies. Further, the angle of the lower frequency region with respect to the horizontal axis signify the capacitive behavior of the electrode (higher the angle, more capacitive in nature). The near vertical shape of the EIS curve for FRMS device indicates superior capacitive behavior compared to other electrode design. Finally, the time constant, τ_0, (which is the time needed to discharge all energy with > 50% efficiency[67-68] is calculated from the impedance phase angle vs. frequency curve to be 20.9 s (LR), 821.4 ms (FR), 615.6 ms (FRNS), and 1.75 ms (FRMS) (Fig.

S9). This shows that the FRMS device is also suitable for deriving instantaneous power and the relaxation time is lower than other reported values such as activated carbon (700 ms),[68] onion-like carbon (26 ms),[22] interdigital graphene/CNT electrodes (4.8 ms).[69]

Further, we investigated the volumetric capacitance of all the devices as a function of current density and shown in Fig. 6c. The specific capacitance decreases with current density. The FRMS device retains more than 50% of its capacitance when operated at an ultrahigh current density of 4,900 mA cm^{-3}. The highest volumetric capacitance of the FRMS electrode was 1224.4 F cm^{-3}, obtained at a current density of 100 mA cm^{-3}; the volumetric capacitance was decreased to a value of 648.3 F cm^{-3} when the current density was increased to 2346 mA cm^{-3}. The lowest volumetric capacitance for the FRMS was still much higher than the highest value obtained from other samples (Fig. 6c). The retention of capacitance as a function of scan rate is shown in Fig. 6d. The volumetric capacitance for the laser reduced sample (LR) dropped dramatically to 25 % of its initial capacitance value by increasing the scan rate from 10 to 50 mV s^{-1} (slope ≈ -17.1% / mV s^{-1}). However, volumetric capacitance for flash reduced samples (FR, FRNS and FRMS) decreased with a milder slope (≈ -4.4% / mV s^{-1}). Interestingly, specific capacitance of FRMS sample retained more than 80 % of its initial capacitance value at higher scan rate of 50 mV s^{-1}. The higher diffusion rate of ions in FRMS sample which is caused due to the high electrolyte wettability of electrodes, is most likely responsible for maintaining the high volumetric capacitance at high scan rates. The capacitance retention of electrodes after being subjected to 5000 charge/discharge cycles is shown in Fig. 6e. FRMS electrode was able to retain 91 % of its initial capacitance after 5000 cycles. However, it is observed that the flash reduced samples (FR, FRNS and FRMS) lose their initial capacitance slightly faster than laser reduced electrode. This is mostly due to the decrease in interlayer spacing of graphene layers after 5000 cycling that reduces the accessible surface area and affects the capacitance retention of active material. However, it could be easily prevented for on-chip and practical energy storage applications by utilizing appropriate designs and use of solid electrolytes.

In order to further evaluate the electrochemical performance of the supercapacitor devices and bulk electrodes, the energy density (E) and power density (P) were calculated from the charge discharge curve using the relationship: $E = \frac{1}{2}CV^2, C = I/(-dV/dt), P = E/t$, where t = time. Figure 6f shows the Ragone plot for different types of interconnected graphene

structures used in this study considering the volume of the active materials at the electrode (calculated from the three electrode tests). It shows that increasing the spacing between graphene layers and increasing the amount of GO to graphene conversion, improves both the energy density and the power density of the electrodes. Moreover, the power density and energy density achievable by FRMS electrodes are roughly three order of magnitude higher than that of LR electrodes. By use of flash reduction instead of laser, energy density was increased from 2 mWh cm^{-3} (LR) to 370 mWh cm^{-3} (FRMS). Similarly, the power density increased five order of magnitudes for the FRMS device compared to the LR device from 0.09 W cm^{-3} (LR) to 416.6 W cm^{-3} (FRMS). In fact, as shown in Fig. 7c, most reported carbon-based supercapacitors shows energy densities <50 mWh cm^{-3}. Figure 7a shows the Ragone plot comparing the different thin-film based energy storage devices. The data includes result from our own devices, commercial supercapacitors tested under the same dynamic conditions [Maxwell Technologies Ultracapacitors (2.7 V/1 F), Cornell Dubilier EDL Supercapacitor (5.5 V/1 F)], and various literature data for batteries [Li thin film battery (4 V/500 μAh),[68] Panasonic Li-ion battery (4.1 V/780 mAh)[70] as well as supercapacitors [electrolytic (3 V/300 μF),[16] graphene-based sandwiched capacitor,[44] graphene-based interdigitated capacitors.[44] FRMS thin-film sandwich-type device showed energy densities of up to 31 mWh/cm^3, which is four times higher than Li thin-film battery (8 mWh cm^{-3}), and four order of magnitude higher than the aluminum electrolytic capacitors (0.0114 mWh cm^{-3}). Further, the energy density of FRMS device is approximately 88 times higher than the state of the art graphene-based sandwich supercapacitors.[44] However, these energy densities are still order of magnitude less than the value obtained by the bulk electrodes (Panasonic Li battery, 403 mWh cm^{-3}). In addition, the power density of the FRMS device (15.3 W cm^{-3}) is 41 times higher than the bulk Li-ion battery (0.37 W cm^{-3}), three order of magnitude higher than the Li thin-film battery (0.005 W cm^{-3}), and two times higher than the state of the art graphene-based sandwich supercapacitors (6.1 W cm^{-3}). Although, the power density of FRMS sandwich-type device is lower than the power density of interdigitated devices (141.8 W cm^{-3}), the device was discharged at much shorter time (1.75 ms) compared to the interdigitated supercapacitor (19 ms). Further, the high power densities are generally observed at lower energy densities. For example, the power density of 137 W cm^{-3} for the aluminum electrolytic capacitor was observed at 0.01 mWh cm^{-3}, and for the in-plane graphene micro-supercapacitor,[28] the power density of 495 W cm^{-3} was observed at an energy

density of 0.14 mWh cm^{-3}. However, the power density of 15.3 W cm^{-3} was observed the FRMS devices even at a higher energy density of 1 mWh cm^{-3}. Finally, our devices outperformed most of the existing bulky as well as thin film based micro-supercapacitors designs reported over the past years (Fig. 7c). The combination of results provided in this paper with recently published designs and studies open up new horizons for practical applications of graphene based structures in countless energy applications and introduce a serious competition for Li-ion batteries.

4. Conclusion

In summary, a novel method for taking advantage of the full potential of graphene based structures through substrate engineered interconnected layers in energy applications has been successfully accomplished. Improved performance in the volumetric capacitance, energy density and power density of graphene based electrodes has been achieved by adjusting the graphene layer inter-spacing and improved diffusion of ions. Furthermore, it is presented that the GO conversion value to graphene is an important consideration while using it as precursor, due to its influence on the electrochemical characterization of electrodes. By controlling the value of GO conversion and interlayer spacing of graphene network, high specific capacitance of 680.2 F g^{-1} was obtained. Likewise, on these electrodes extremely high energy density of 370 mWh cm^{-3} was obtained along with a high power density of 416.6 W cm^{-3}. Above all, these modifications are applied by means of flash reduction process of GO and patterning of transparent PET substrate. Thus, the whole process is cost efficient, faster and amenable to scale-up for practical electrochemical energy storage applications.

Supporting Information

Detailed procedure of sample preparation; electrical conductivity measurement; cross-sectional SEM; BET surface area; FTIR-ATR measurement.

Acknowledgments

The research reported here was supported, in part, by the Louisiana Board of Regents through the Board of Regents Support Fund (Contract Number: LEQSF(2017-20)-RD-A-04 and LEQSF(2017-18)-ENH-TR-08), National Science Foundation (Award Number: 1660233) and U.S. Department of Energy (DOE) Bioenergy Technologies Office (BETO) and Vehicles Technologies Office (VTO) under the DOE Co-Optimization of Fuels and Engines Initiative

(Project number: DE-EE0007981). M.R.G. thanks Louisiana State University start-up funds for partially supporting the research. We sincerely appreciate Z. Xie and W. Xu for their assistance with electrochemical experiments and impedance measurements.

References

(1) Chee, W. K.; Lim, H. N.; Zainal, Z.; Huang, N. M.; Harrison, I.; Andou, Y. Flexible graphene-based supercapacitors: a review. *J. Phys. Chem. C* **2016,** *120* (8), 4153-4172.

(2) Shao, Y.; El-Kady, M. F.; Wang, L. J.; Zhang, Q.; Li, Y.; Wang, H.; Mousavi, M. F.; Kaner, R. B. Graphene-based materials for flexible supercapacitors. *Chem. Soc. Rev.* **2015,** *44* (11), 3639-3665.

(3) Xiong, G.; Meng, C.; Reifenberger, R. G.; Irazoqui, P. P.; Fisher, T. S. A review of graphene□based electrochemical microsupercapacitors. *Electroanal.* **2014,** *26* (1), 30-51.

(4) Wu, Z.-S.; Feng, X.; Cheng, H.-M. Recent advances in graphene-based planar micro-supercapacitors for on-chip energy storage. *Natl. Sci. Rev.* **2014,** *1* (2), 277-292.

(5) Kim, T.; Jung, G.; Yoo, S.; Suh, K. S.; Ruoff, R. S. Activated graphene-based carbons as supercapacitor electrodes with macro-and mesopores. *ACS Nano* **2013,** *7* (8), 6899-6905.

(6) Lin, J.; Zhang, C.; Yan, Z.; Zhu, Y.; Peng, Z.; Hauge, R. H.; Natelson, D.; Tour, J. M. 3-dimensional graphene carbon nanotube carpet-based microsupercapacitors with high electrochemical performance. *Nano Lett.* **2012,** *13* (1), 72-78.

(7) Wang, H.; Yi, H.; Chen, X.; Wang, X. Asymmetric supercapacitors based on nano-architectured nickel oxide/graphene foam and hierarchical porous nitrogen-doped carbon nanotubes with ultrahigh-rate performance. *J. Mater. Chem. A* **2014,** *2* (9), 3223-3230.

(8) Yan, J.; Fan, Z.; Wei, T.; Qian, W.; Zhang, M.; Wei, F. Fast and reversible surface redox reaction of graphene–MnO 2 composites as supercapacitor electrodes. *Carbon* **2010,** *48* (13), 3825-3833.

(9) Gu, W.; Yushin, G. Review of nanostructured carbon materials for electrochemical capacitor applications: advantages and limitations of activated carbon, carbide□derived carbon, zeolite□templated carbon, carbon aerogels, carbon nanotubes, onion□like carbon, and graphene. *Wiley Interdiscip. Rev. Energy Environ.* **2014,** *3* (5), 424-473.

(10) Li, C.; Shi, G. Three-dimensional graphene architectures. *Nanoscale* **2012,** *4* (18), 5549-5563.

(11) Qu, L.; Zhao, Y.; Khan, A. M.; Han, C.; Hercule, K. M.; Yan, M.; Liu, X.; Chen, W.; Wang, D.; Cai, Z. Interwoven Three-Dimensional Architecture of Cobalt Oxide Nanobrush-Graphene@ Ni x Co2 x (OH) 6 x for High-Performance Supercapacitors. *Nano Lett.* **2015,** *15* (3), 2037-2044.

(12) Sun, H.; Mei, L.; Liang, J.; Zhao, Z.; Lee, C.; Fei, H.; Ding, M.; Lau, J.; Li, M.; Wang, C. Three-dimensional holey-graphene/niobia composite architectures for ultrahigh-rate energy storage. *Science* **2017,** *356* (6338), 599-604.

(13) Xu, Z.; Li, Z.; Holt, C. M.; Tan, X.; Wang, H.; Amirkhiz, B. S.; Stephenson, T.; Mitlin, D. Electrochemical supercapacitor electrodes from sponge-like graphene nanoarchitectures with ultrahigh power density. *J. Phys. Chem. Lett.* **2012,** *3* (20), 2928-2933.

(14) Yoon, Y.; Lee, K.; Kwon, S.; Seo, S.; Yoo, H.; Kim, S.; Shin, Y.; Park, Y.; Kim, D.; Choi, J.-Y. Vertical alignments of graphene sheets spatially and densely piled for fast ion diffusion in compact supercapacitors. *ACS Nano* **2014,** *8* (5), 4580-4590.

(15) Huang, X.; Zeng, Z.; Fan, Z.; Liu, J.; Zhang, H. Graphene□based electrodes. *Adv. Mater.* **2012,** *24* (45), 5979-6004.

(16) El-Kady, M. F.; Strong, V.; Dubin, S.; Kaner, R. B. Laser scribing of high-performance and flexible graphene-based electrochemical capacitors. *Science* **2012,** *335* (6074), 1326-1330.

(17) Chen, T.; Xue, Y.; Roy, A. K.; Dai, L. Transparent and stretchable high-performance supercapacitors based on wrinkled graphene electrodes. *ACS Nano* **2013,** *8* (1), 1039-1046.

(18) Chen, J.; Li, C.; Shi, G. Graphene materials for electrochemical capacitors. *J. Phys. Chem. Lett.* **2013,** *4* (8), 1244-1253.

(19) Luo, J.; Jang, H. D.; Huang, J. Effect of sheet morphology on the scalability of graphene-based ultracapacitors. *ACS Nano* **2013,** *7* (2), 1464-1471.

(20) Basnayaka, P. A.; Ram, M. K. A Review of Supercapacitor Energy Storage Using Nanohybrid Conducting Polymers and Carbon Electrode Materials. In *Conducting Polymer Hybrids*; Springer: 2017; pp 165-192.

(21) Cote, L. J.; Cruz-Silva, R.; Huang, J. Flash reduction and patterning of graphite oxide and its polymer composite. *J. Am. Chem. Soc.* **2009,** *131* (31), 11027-11032.

(22) Kyerematen, N. A.; Brousse, T.; Pech, D. Microsupercapacitors as miniaturized energy-storage components for on-chip electronics. *Nat. Nanotechnol.* **2017,** *12* (1), 7-15.

(23) Lee, J. H.; Park, N.; Kim, B. G.; Jung, D. S.; Im, K.; Hur, J.; Choi, J. W. Restacking-inhibited 3D reduced graphene oxide for high performance supercapacitor electrodes. *ACS Nano* **2013,** *7* (10), 9366-9374.

(24) Zhang, L.; Zhang, F.; Yang, X.; Long, G.; Wu, Y.; Zhang, T.; Leng, K.; Huang, Y.; Ma, Y.; Yu, A. Porous 3D graphene-based bulk materials with exceptional high surface area and excellent conductivity for supercapacitors. *Sci. Rep.* **2013,** *3*, 1408.

(25) Zhu, Y.; Li, L.; Zhang, C.; Casillas, G.; Sun, Z.; Yan, Z.; Ruan, G.; Peng, Z.; Raji, A.-R. O.; Kittrell, C. A seamless three-dimensional carbon nanotube graphene hybrid material. *Nat. Commun.* **2012,** *3*, 1225.

(26) Goh, M. S.; Pumera, M. Multilayer graphene nanoribbons exhibit larger capacitance than their few-layer and single-layer graphene counterparts. *Electrochem. Commun.* **2010,** *12* (10), 1375-1377.

(27) Xia, J.; Chen, F.; Li, J.; Tao, N. Measurement of the quantum capacitance of graphene. *Nat. Nanotechnol.* **2009,** *4* (8), 505-509.

(28) Wu, Z. S.; Parvez, K.; Feng, X.; Müllen, K. Graphene-based in-plane micro-supercapacitors with high power and energy densities. *Nat. Commun.* **2013,** *4*.

(29) Zhu, Y.; Murali, S.; Stoller, M. D.; Ganesh, K.; Cai, W.; Ferreira, P. J.; Pirkle, A.; Wallace, R. M.; Cychosz, K. A.; Thommes, M. Carbon-based supercapacitors produced by activation of graphene. *Science* **2011,** *332* (6037), 1537-1541.

(30) Chen, T.; Dai, L. Carbon nanomaterials for high-performance supercapacitors. *Mater. Today* **2013,** *16* (7), 272-280.

(31) Pham, D. T.; Lee, T. H.; Luong, D. H.; Yao, F.; Ghosh, A.; Le, V. T.; Kim, T. H.; Li, B.; Chang, J.; Lee, Y. H. Carbon nanotube-bridged graphene 3D building blocks for ultrafast compact supercapacitors. *ACS Nano* **2015,** *9* (2), 2018-2027.

(32) Xie, B.; Yang, C.; Zhang, Z.; Zou, P.; Lin, Z.; Shi, G.; Yang, Q.; Kang, F.; Wong, C.-P. Shape-tailorable graphene-based ultra-high-rate supercapacitor for wearable electronics. *ACS Nano* **2015,** *9* (6), 5636-5645.

(33) Liu, J. Charging graphene for energy. *Nat. Nanotechnol.* **2014,** *9* (10), 739-741.

(34) Ke, Q.; Wang, J. Graphene-based materials for supercapacitor electrodes–A review. *J Materiomics* **2016,** *2* (1), 37-54.

(35) Wang, Y.; Shi, Z.; Huang, Y.; Ma, Y.; Wang, C.; Chen, M.; Chen, Y. Supercapacitor devices based on graphene materials. *J. Phys. Chem. C* **2009,** *113* (30), 13103-13107.

(36) Liu, C.; Yu, Z.; Neff, D.; Zhamu, A.; Jang, B. Z. Graphene-based supercapacitor with an ultrahigh energy density. *Nano Lett.* **2010,** *10* (12), 4863-4868.

(37) Simon, P.; Gogotsi, Y. Materials for electrochemical capacitors. *Nat. Mater.* **2008,** *7* (11), 845-854.

(38) Xiao, N.; Tan, H.; Zhu, J.; Tan, L.; Rui, X.; Dong, X.; Yan, Q. High-performance supercapacitor electrodes based on graphene achieved by thermal treatment with the aid of nitric acid. *ACS Appl. Mater. Interfaces* **2013,** *5* (19), 9656-9662.

(39) Zheng, H.; Yang, G.; Chen, S.; Jia, Y. Hydrothermal Synthesis of 3D Porous Structure Bi2WO6/Reduced Graphene Oxide Hydrogels for Enhancing Supercapacitor Performance. *ChemElectroChem* **2017,** *4* (3), 577-584.

(40) Zhang, H.; Yang, J.; Hou, H.; Chen, S.; Yao, H. Nitrogen-doped carbon paper with 3D porous structure as a flexible free-standing anode for lithium-ion batteries. *Sci. Rep.* **2017,** *7* (1), 7769.

(41) Wang, C.-C.; Liang, J.; Liao, Y.-H.; Lu, S.-Y. 3D porous graphene nanostructure from a simple, fast, scalable process for high performance flexible gel-type supercapacitors. *ACS Sustain. Chem. Eng.* **2017,** *5* (5), 4457-4467.

(42) Wen, F.; Hao, C.; Xiang, J.; Wang, L.; Hou, H.; Su, Z.; Hu, W.; Liu, Z. Enhanced laser scribed flexible graphene-based micro-supercapacitor performance with reduction of carbon nanotubes diameter. *Carbon* **2014,** *75*, 236-243.

(43) Yang, D.; Bock, C. Laser reduced graphene for supercapacitor applications. *J. Power Sources* **2017,** *337*, 73-81.

(44) El-Kady, M. F.; Kaner, R. B. Scalable fabrication of high-power graphene micro-supercapacitors for flexible and on-chip energy storage. *Nat. Commun.* **2013,** *4*, 1475.

(45) Wu, Z. S.; Parvez, K.; Li, S.; Yang, S.; Liu, Z.; Liu, S.; Feng, X.; Müllen, K. Alternating Stacked Graphene□Conducting Polymer Compact Films with Ultrahigh Areal and Volumetric Capacitances for High□Energy Micro□Supercapacitors. *Adv. Mater.* **2015,** *27* (27), 4054-4061.

(46) Raccichini, R.; Varzi, A.; Passerini, S.; Scrosati, B. The role of graphene for electrochemical energy storage. *Nat. Mater.* **2015,** *14* (3), 271-279.

(47) Yu, D.; Goh, K.; Wang, H.; Wei, L.; Jiang, W.; Zhang, Q.; Dai, L.; Chen, Y. Scalable synthesis of hierarchically structured carbon nanotube-graphene fibres for capacitive energy storage. *Nat. Nanotechnol.* **2014,** *9* (7), 555-562.

(48) Xu, Y.; Lin, Z.; Zhong, X.; Huang, X.; Weiss, N. O.; Huang, Y.; Duan, X. Holey graphene frameworks for highly efficient capacitive energy storage. *Nat. Commun.* **2014,** *5*, 4554.

(49) Han, S.; Wu, D.; Li, S.; Zhang, F.; Feng, X. Porous graphene materials for advanced electrochemical energy storage and conversion devices. *Adv. Mater.* **2014,** *26* (6), 849-864.

(50) Zhao, H.; Liu, L.; Vellacheri, R.; Lei, Y. Recent Advances in Designing and Fabricating Self□Supported Nanoelectrodes for Supercapacitors. *Adv. Sci.* **2017,** *4* (10), 34.

(51) Homenick, C. M.; James, R.; Lopinski, G. P.; Dunford, J.; Sun, J.; Park, H.; Jung, Y.; Cho, G.; Malenfant, P. R. Fully printed and encapsulated SWCNT-based thin film transistors via a combination of R2R gravure and inkjet printing. *ACS Appl. Mater. Interfaces* **2016,** *8* (41), 27900-27910.

(52) Liu, Z.; Liu, S.; Dong, R.; Yang, S.; Lu, H.; Narita, A.; Feng, X.; Müllen, K. High Power In□Plane Micro□Supercapacitors Based on Mesoporous Polyaniline Patterned Graphene. *Small* **2017,** *13* (14).

(53) Kaniyoor, A.; Ramaprabhu, S. A Raman spectroscopic investigation of graphite oxide derived graphene. *AIP Adv.* **2012,** *2* (3), 032183.

(54) Johra, F. T.; Lee, J.-W.; Jung, W.-G. Facile and safe graphene preparation on solution based platform. *Ind. Eng. Chem. Res.* **2014,** *20* (5), 2883-2887.

(55) Mishra, S. K.; Tripathi, S. N.; Choudhary, V.; Gupta, B. D. SPR based fibre optic ammonia gas sensor utilizing nanocomposite film of PMMA/reduced graphene oxide prepared by in situ polymerization. *Sensor Actuat. B Chem.* **2014,** *199*, 190-200.

(56) Lu, W.; Liu, S.; Qin, X.; Wang, L.; Tian, J.; Luo, Y.; Asiri, A. M.; Al-Youbi, A. O.; Sun, X. High-yield, large-scale production of few-layer graphene flakes within seconds: using chlorosulfonic acid and H 2 O 2 as exfoliating agents. *J. Mater. Chem.* **2012,** *22* (18), 8775-8777.

(57) Dikin, D. A.; Stankovich, S.; Zimney, E. J.; Piner, R. D.; Dommett, G. H.; Evmenenko, G.; Nguyen, S. T.; Ruoff, R. S. Preparation and characterization of graphene oxide paper. *Nature* **2007,** *448* (7152), 457-460.

(58) Buchsteiner, A.; Lerf, A.; Pieper, J. Water dynamics in graphite oxide investigated with neutron scattering. *J. Phys. Chem. B* **2006,** *110* (45), 22328-22338.

(59) Lerf, A.; Buchsteiner, A.; Pieper, J.; Schöttl, S.; Dekany, I.; Szabo, T.; Boehm, H. Hydration behavior and dynamics of water molecules in graphite oxide. *J. Phys. Chem. Solids* **2006,** *67* (5), 1106-1110.

(60) Fang, S.; Huang, D.; Lv, R.; Bai, Y.; Huang, Z.-H.; Gu, J.; Kang, F. Three-dimensional reduced graphene oxide powder for efficient microwave absorption in the S-band (2–4 GHz). *RSC Adv.* **2017,** *7* (41), 25773-25779.

(61) Fan, Z.; Wang, K.; Wei, T.; Yan, J.; Song, L.; Shao, B. An environmentally friendly and efficient route for the reduction of graphene oxide by aluminum powder. *Carbon* **2010,** *48* (5), 1686-1689.

(62) Tung, V. C.; Allen, M. J.; Yang, Y.; Kaner, R. B. High-throughput solution processing of large-scale graphene. *Nat. Nanotechnol.* **2009,** *4* (1), 25-29.

(63) Vollebregt, S.; Ishihara, R.; Tichelaar, F.; Hou, Y.; Beenakker, C. Influence of the growth temperature on the first and second-order Raman band ratios and widths of carbon nanotubes and fibers. *Carbon* **2012,** *50* (10), 3542-3554.

(64) Claramunt, S.; Varea, A.; López-Díaz, D.; Velázquez, M. M.; Cornet, A.; Cirera, A. The importance of interbands on the interpretation of the Raman spectrum of graphene oxide. *J. Phys. Chem. C* **2015,** *119* (18), 10123-10129.

(65) Zhu, Y.; Murali, S.; Cai, W.; Li, X.; Suk, J. W.; Potts, J. R.; Ruoff, R. S. Graphene and graphene oxide: synthesis, properties, and applications. *Adv. Mater.* **2010,** *22* (35), 3906-3924.

(66) Stoller, M. D.; Park, S.; Zhu, Y.; An, J.; Ruoff, R. S. Graphene-based ultracapacitors. *Nano Lett.* **2008,** *8* (10), 3498-3502.

(67) Taberna, P.; Simon, P.; Fauvarque, J.-F. Electrochemical characteristics and impedance spectroscopy studies of carbon-carbon supercapacitors. *J. Electrochem. Soc.* **2003,** *150* (3), A292-A300.

(68) Pech, D.; Brunet, M.; Durou, H.; Huang, P.; Mochalin, V.; Gogotsi, Y.; Taberna, P.-L.; Simon, P. Ultrahigh-power micrometre-sized supercapacitors based on onion-like carbon. *Nat. Nanotechnol.* **2010,** *5* (9), 651-654.

(69) Beidaghi, M.; Wang, C. Micro□supercapacitors based on interdigital electrodes of reduced graphene oxide and carbon nanotube composites with ultrahigh power handling performance. *Adv. Funct. Mater.* **2012,** *22* (21), 4501-4510.

(70) Nagasubramanian, G.; Jungst, R.; Doughty, D. Impedance, power, energy, and pulse performance characteristics of small commercial Li-ion cells. *J. Power Sources* **1999,** *83* (1), 193-203.

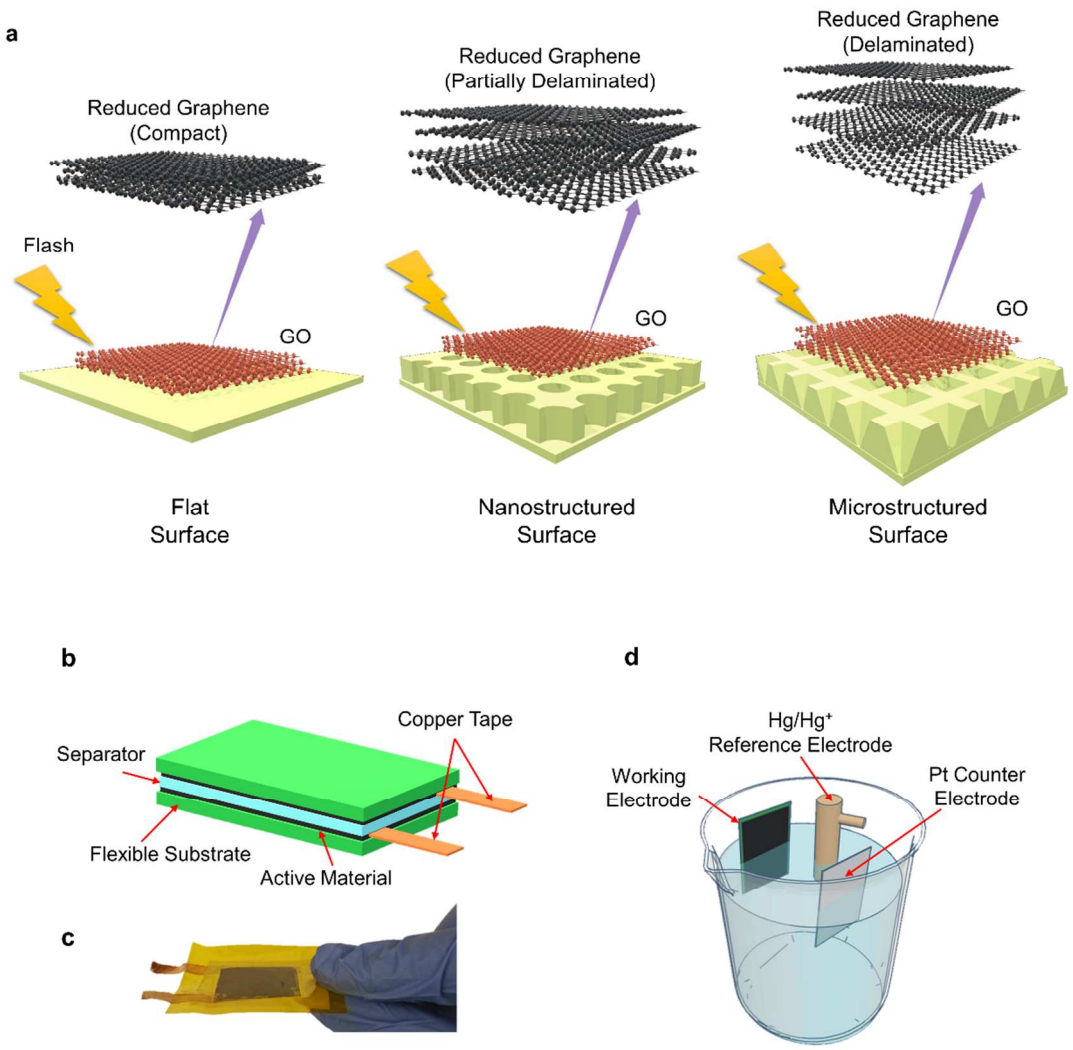

Figure 1. Schematic illustration of substrate engineering effect on electrodes for energy applications using flash reduction on flat and patterned substrates. (a) By means of substrate engineering, interlayer spacing of graphene layers increases considerably. Therefore, the diffusion of electrolyte into the interconnected graphene structure is facilitated. (b) Schematic image of the device. (c) Image of the device made by FRMS electrodes. (d) Schematic image of the three electrode configuration used in the electrochemical experiments.

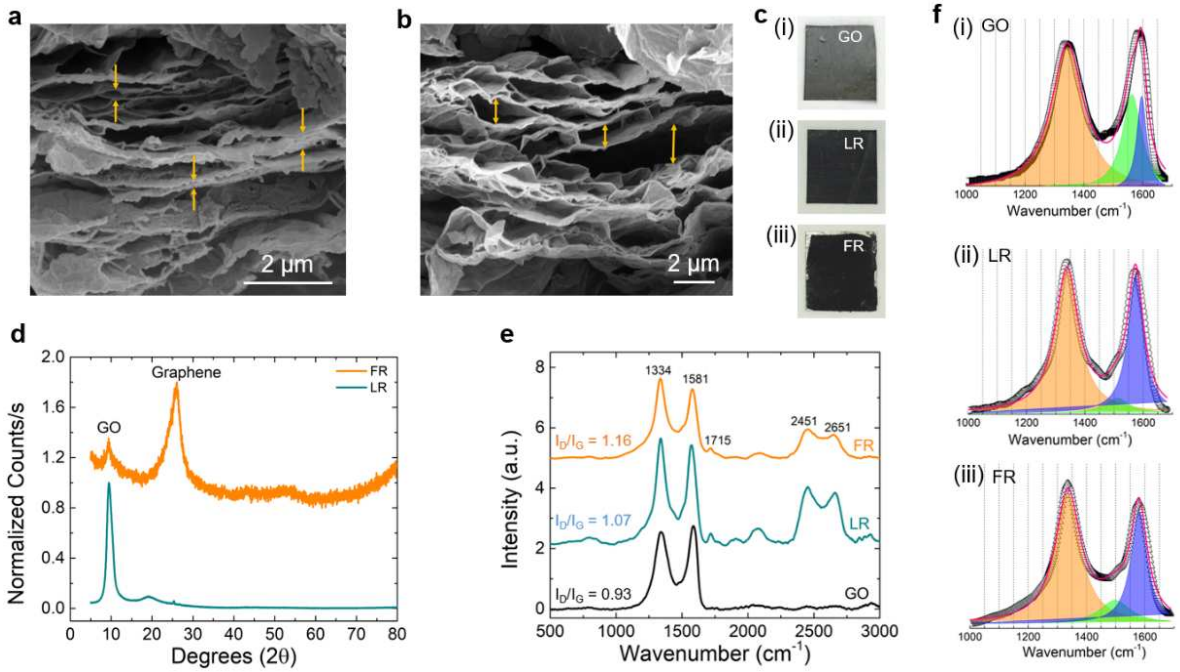

Figure 2. Comparison of (a, b) SEM images, (c) bright-field images, (d) XRD analysis and (e, f) Raman spectra of graphene produced by laser reduction and flash reduction methods. (a) SEM image of laser reduced sample shows agglomerated compact layers of graphene sheets with the average interlayer spacing of 0.25 μm. (b) SEM image of flash reduced sample illustrates the delaminated layers of graphene sheets with the mean spacing of 1.76 μm. (c) Bright field images of laser and flash reduced samples apparently show the color change from brown (in GO) to black (in LR and FR) after laser and flash reduction methods. (d) XRD results show a considerable amount of residual GO ($I_{GO}/I_{Graphene} \approx 11.14$) after performing the laser reduction (LR) technique. Meanwhile, the value of residual GO remarkably decreased by an order of magnitude ($I_{GO}/I_{Graphene} \approx 0.77$) by using of flash reduction (FR) method. In order to adhere LR sample to sample holder, a thin layer of Vaseline was used. (e, f) Comparison of the Raman spectra of GO, LR, and FR samples. The D and G-band for each sample is deconvoluted into three peaks.

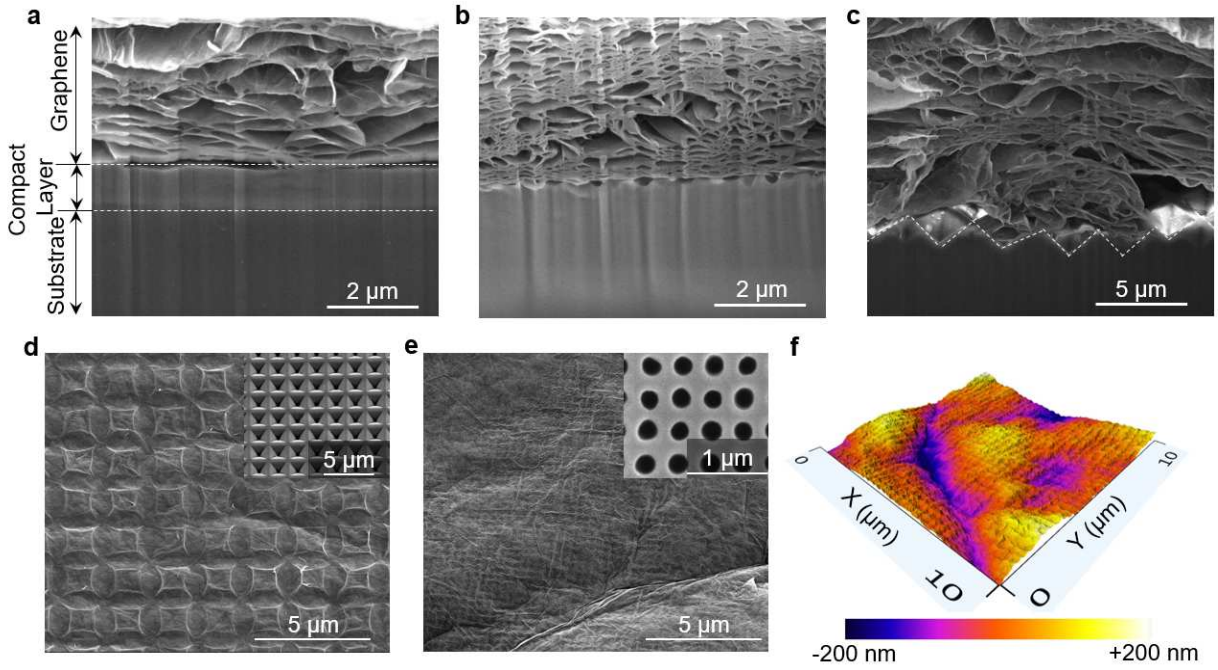

Figure 3. Comparison of cross sectional and top view SEM images of electrodes produced using flash reduction method on flat, nano and micro structure substrates showing the effect of substrate engineering. (a) SEM image of flash reduced on flat (FR) sample shows a compact layer of graphene sheets. (b) SEM images of flash reduced on nano structure (FRNS) electrode illustrate that the thickness of graphene compact layers considerably decreased, but the bottom layers are not still as delaminated as top layers. (c) SEM images of flash reduced GO on micro structure (FRMS) electrode show the uniformly delaminated layers of graphene from bottom to top. (d) SEM image of GO on microstructured substrate before the reduction process. The inset shows the geometry of the inverse pyramid structure of the substrate with pitch of 2 µm, pit length of 1.5 µm and pit depth of 2.1 µm. (e) SEM image of GO on nano substrate before the reduction process. The inset shows the geometry of the periodic nanohole structure of the substrate with pitch of 350 nm, hole diameter of 180 nm and hole depth of 0.5 µm. (f) AFM analysis confirms the formation of a nanostructured pattern on GO before reduction on nanostructured substrate.

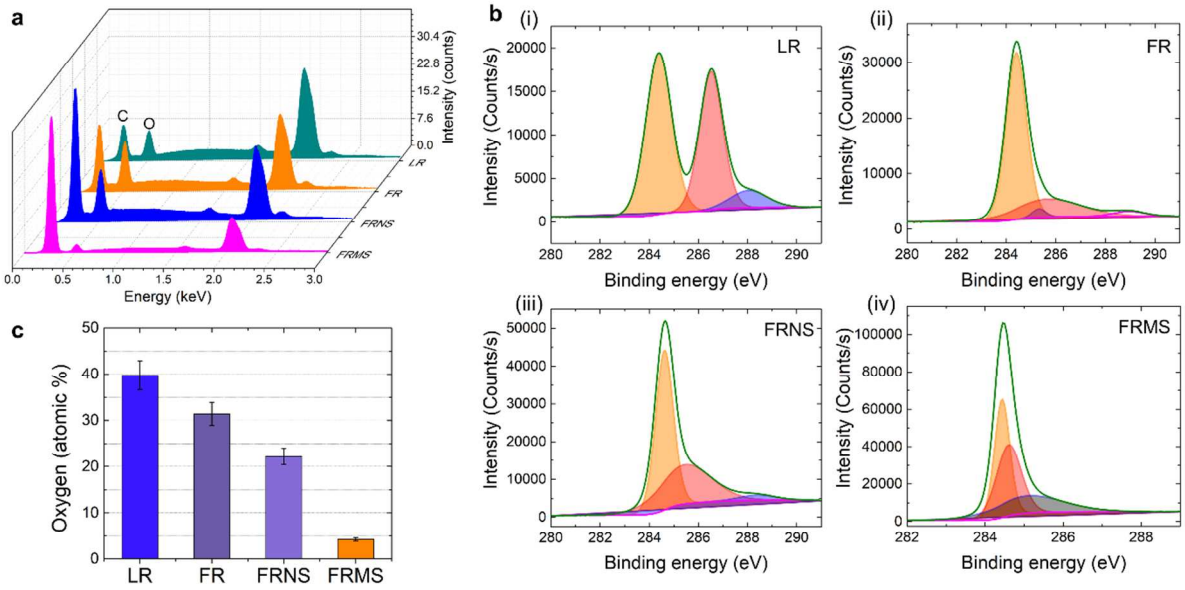

Figure 4. EDS analysis and XPS spectra of C 1s in LR, FR, FRNS and FRMS electrodes. (a) EDS analysis shows a dramatic difference in the oxygen and carbon content of samples. (b) XPS results for (i) LR, (ii) FR, (iii) FRNS and (iv) FRMS electrodes confirm the enhanced conversion of GO to graphene while using flash reduction method on patterned substrates. Deconvolution of the XPS peak in to four peaks showed the different oxygen containing functional groups. (c) LR electrode shows the highest amount of residual oxygen (39.8 %) and FRMS sample represents the lowest value (4.2 %). The amount of residual oxygen decreases dramatically from LR to FRMS sample.

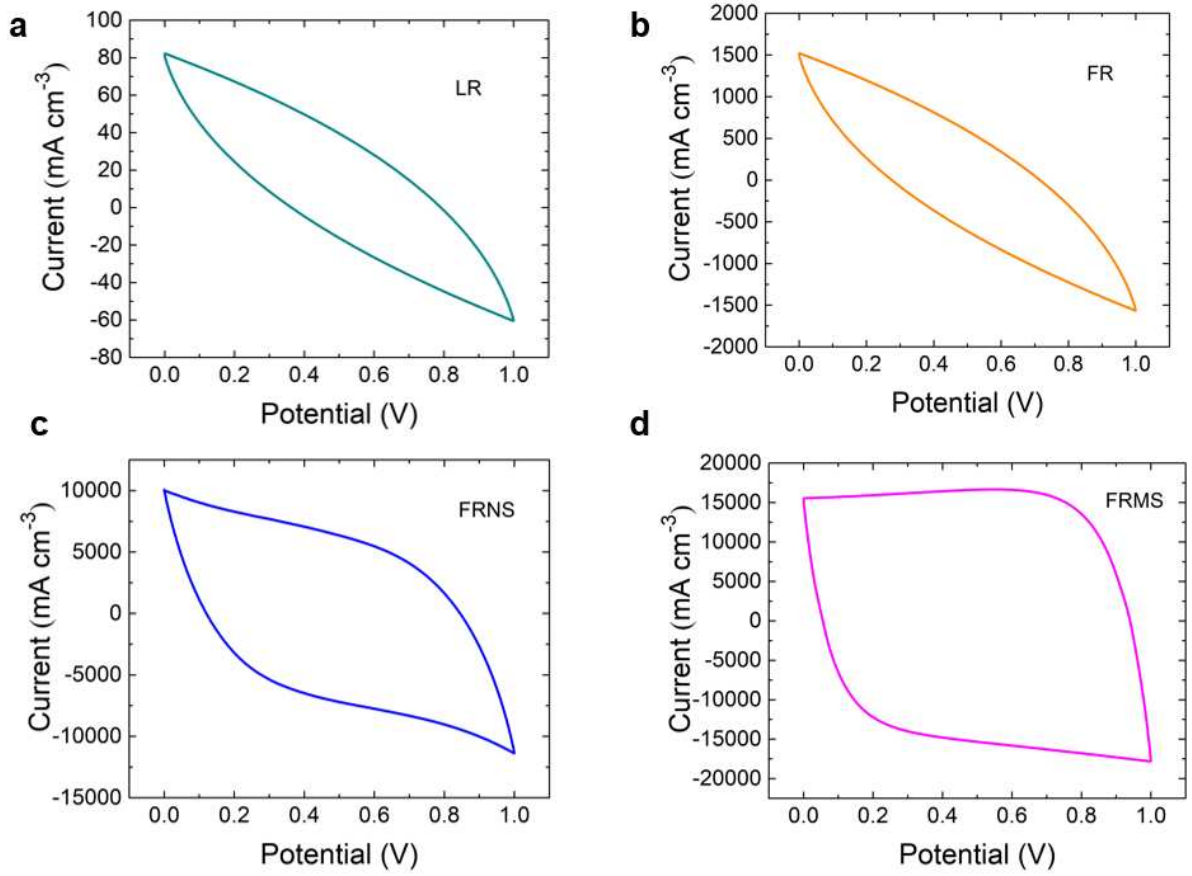

Figure 5. Cyclic voltammetry (CV) curves of (a) LR, (b) FR, (c) FRNS and (d) FRMS samples at scan rate of 100 mV s^{-1}. The integrated area of each cycle is correlated with the value of capacitance and increases from LR to FRMS electrode by orders of magnitude. FRMS CV curve reveals a rectangular shape that confirms the swift current response by voltage change.

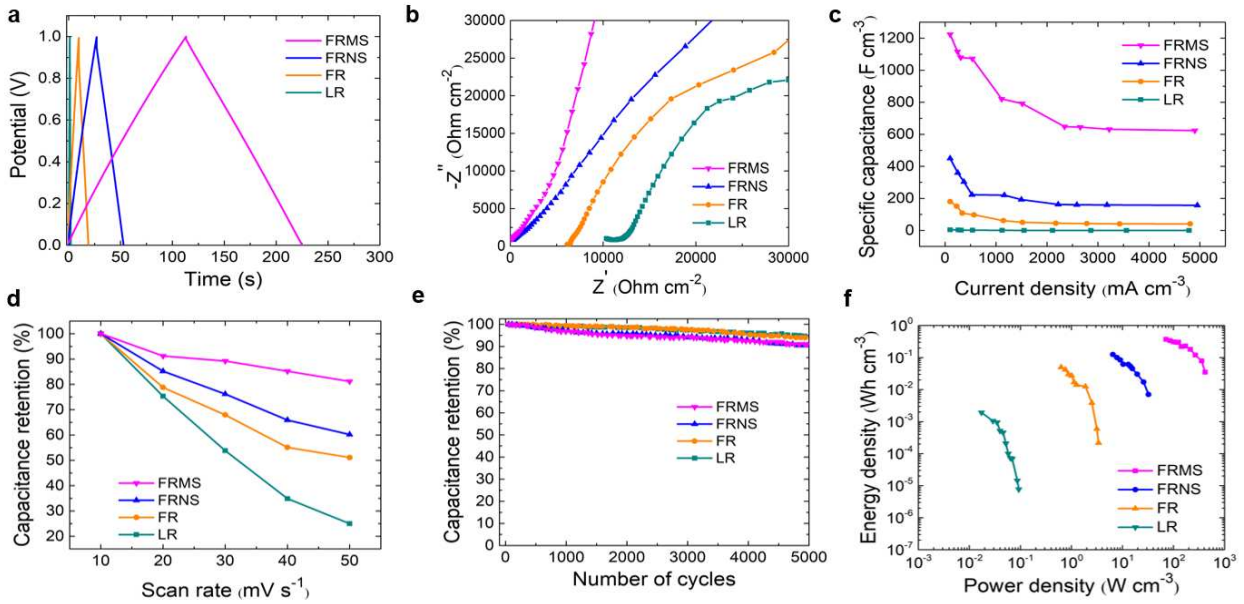

Figure 6. Electrochemical performance of LR, FR, FRNS and FRMS electrodes. (a) Galvanostatic charge/discharge curves at the current density of 100 mA cm^{-3}, shows a dramatic difference in the discharge time of various electrodes. FRMS electrode illustrates the highest double layer capacitance. (b) Nyquist plot shows the complex plane plot of impedance for four different electrodes. Due to the lowest equivalent series resistance, FRMS electrode is the most appropriate choice for on-chip applications. (c) Plot showing the volumetric capacitance evolution as a function of the current density confirms the functionality of FRMS electrode at high current densities. (d) Evolution of specific capacitance vs. scan rate shows the highest diffusion rate in FRMS sample compared to FRNS, FR and LR electrodes. (e) Reliability plot of different electrodes shows the stability of substrate engineered electrodes for 5000 cycles. (f) Ragone plot confirms that the FRMS electrode demonstrates the highest energy and power densities compared to FRNS, FR and LR samples.

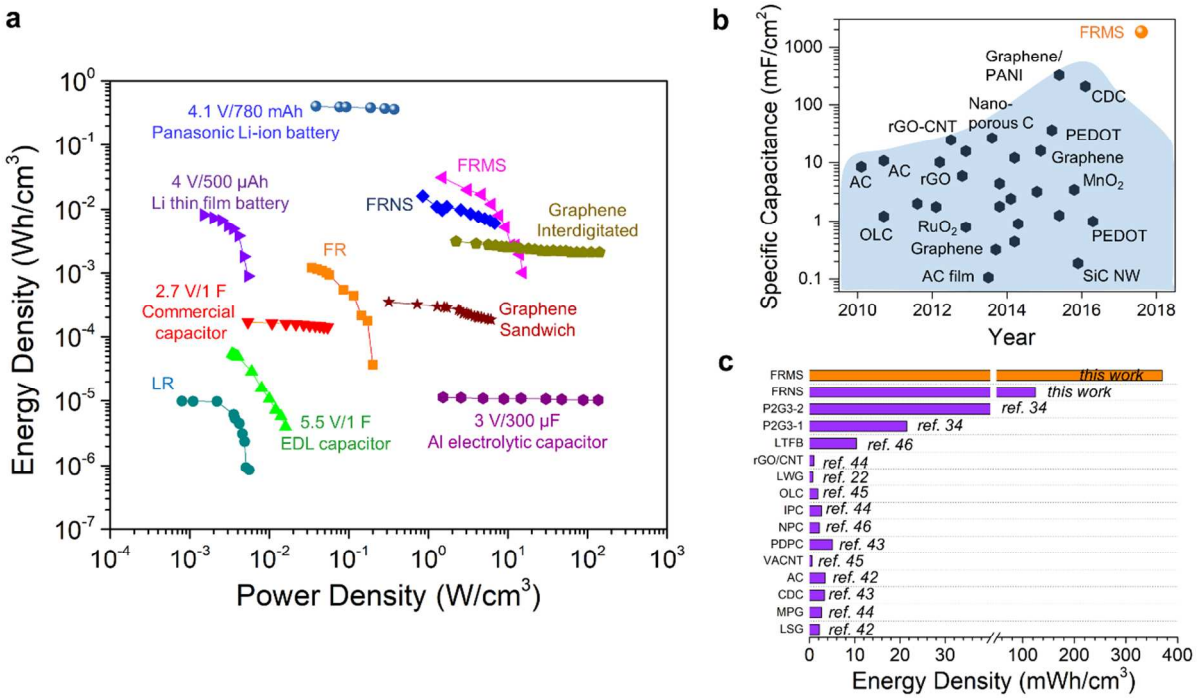

Figure 7. Comparison of FRMS electrode properties with several commercial and conventional energy storage devices. (a) FRMS electrode exhibits ultra-high energy and power densities compared to Li thin-film batteries, graphene interdigitated thin film supercapacitor and several other high-end energy storage devices. (b) FRMS electrode shows an ultra-high specific areal capacitance that makes it suitable for flexible and wearable electronics. The value of areal capacitance for FRMS electrode is approximately 5.6 times larger than Graphene/PANI electrodes (c) FRMS electrode shows the highest value of energy density (370 mWh cm^{-3}), among the carbon based electrodes. So far, the energy density obtained from carbon based electrodes are limited to ~ 50 mWh cm^{-3}. Here, AC: Activated Carbon;[22, 31] OLC: Onion-like Carbon;[42] rGO: Reduced Graphene Oxide;[31, 42, 43] CNT: Carbon Nanotube;[42] CDC: Carbide Derived Carbon;[44] PEDOT: Polyethylenedioxythiophene;[45] NW: Nanowire;[44, 45] FRMS: Flash Reduced Microstructure; PANI: Polyaniline.[43]

Table of Contents (TOC)

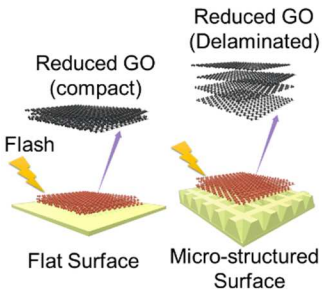

For Table of Contents Only